ACCSCIENCE PUBLISHING

International Journal of Bioprinting

RESEARCH ARTICLE

Three-dimensional-printed hydroxyapatite/zirconium dioxide composite scaffold incorporating bone morphogenetic protein-2 for lumbar vertebral bone defect repair in rhesus macaques

Rui Qiu[1], Hua-Teng Zhou[2], Ren-Fu Quan[2]*, Can-Da Xu[2], Tuo Wang[2], Wei-Bin Du[2], Huan-Huan Gao[2], Xiao-Long Huang[2], Cai-Yin Xu[3], Long-Bao Lv[3], Xi-Cheng Wei[4], and Jin-Fu Wang[5]

[1] Department of Orthopedic Surgery, Huang Jia Si Hospital of Yushan County (Yushan People's Hospital), Shangrao, Jiangxi, China

[2] Department of Orthopedics, Affiliated Jiangnan Hospital of Zhejiang Chinese Medical University, Hangzhou, Zhejiang, China

[3] Kunming Institute of Zoology, Chinese Academy of Sciences, Kunming, Yunnan, China

[4] Department of Polymer Materials, School of Materials Science and Engineering, Shanghai University, Shanghai, China

[5] Institute of Cell and Development, College of Life Sciences, Zhejiang University, Hangzhou, Zhejiang, China

***Corresponding author:**
Ren-Fu Quan
(quanrenfu@126.com)

Citation: Qiu R, Zhou HT, Quan RF, *et al*. Three-dimensional-printed hydroxyapatite/zirconium dioxide composite scaffold incorporating bone morphogenetic protein-2 for lumbar vertebral bone defect repair in rhesus macaques. *Int J Bioprint*. 2026;12(1):467-484. doi: 10.36922/IJB025390400

Received: September 26, 2025
Revised: November 30, 2025
Accepted: December 9, 2025
Published online: December 18, 2025

Abstract

Bone defects caused by various factors have become a persistent challenge in orthopedic clinics, and traditional treatment methods mainly involve the use of artificial bone or autologous bone transplantation. However, these methods have considerable limitations, such as donor site bone loss, immune rejection, and the risk of secondary infection at the donor site. Therefore, considering these limitations and the rapid development of the field of bone tissue engineering, this study adopted light-curing stereolithography three-dimensional (3D) printing technology to design bone scaffold materials. The technology was used to prepare hydroxyapatite (HA)/zirconium dioxide (ZrO_2) porous composites with satisfactory mechanical properties as tissue-engineering bone scaffolds. A bone morphogenetic protein-2-loaded gelatin/chitosan hydrogel sustained-release system was prepared via an emulsification and cross-linking process. Subsequently, rhesus macaque bone marrow mesenchymal stem cells, acting as osteogenic progenitors, were seeded into the system. Novel HA/ZrO2 scaffolds were fabricated using stereolithography 3D printing technology to serve as bone graft substitutes. The resulting scaffold exhibited a 3D interconnected porous structure and showed good biocompatibility and osteoinductive ability in a rhesus macaque lumbar vertebral bone defect model. The results confirmed that the scaffold achieved osteogenic efficiency comparable to that of autologous bone grafting in rhesus macaques. Therefore, the developed scaffold material has promising potential in bone defect repair.

Keywords: Hydroxyapatite; Nanomaterials; Three-dimensional printing; Tissue-engineered bone; Vertebral defect; Zirconium dioxide

1. Introduction

As an important branch of regenerative medicine, bone tissue engineering aims to construct functional bone tissue by combining biomaterials, cells, and growth factors to repair large-scale bone defects and to overcome the limitations of traditional transplantation techniques. Remarkable progress has been made in this field in terms of osteogenic mechanisms, material innovation, and clinical translation.[1,2] The application of three-dimensional (3D) printing technology in bone tissue engineering has also shown considerable potential and diverse advancements. By precisely manipulating the macroscopic and microscopic structures of the scaffold, this technology can be used to fabricate a bone defect repair scaffold with biomimetic pore size, porosity, and connectivity similar to that of natural bone, which can effectively promote cell adhesion, proliferation, and new bone generation.[3,4] Various biomaterials have been widely researched and developed as bone substitutes.

In the present study, a hydroxyapatite (HA)/zirconium dioxide (ZrO_2) composite scaffold material with a favorable surface morphology and a unique 3D interconnected porous structure was prepared using light-curing stereolithography (SLA) 3D-printing technology. The hydroxyapatite component is similar to natural apatite mineral and is the main inorganic component of vertebrate bone and teeth. After implantation, it partially degrades, releasing calcium and phosphorus ions that are reabsorbed and utilized by the body, thereby promoting effective integration with the host bone.[5] The ZrO_2 component improves the mechanical strength of the material and provides resistance to biodegradation, thereby conferring long-term biostability. The inclusion of ZrO_2 substantially improves the fracture toughness of the material and establishes a strong biological connection at the bone interface.[6] Bone morphogenetic protein 2 (BMP-2) is one of the most potent known osteogenic inducers and directly induces osteoblast (OB) differentiation and bone formation. Moreover, BMP-2 upregulates the expression of vascular endothelial growth factor (VEGF) in a concentration- and time-dependent manner during the induction of osteogenic precursor cell differentiation, thereby promoting vascularization and angiogenesis.[7] VEGF not only enhances the recruitment and survival of mesenchymal stem cells by promoting the formation of vascular networks but also enhances the osteogenic response of mesenchymal stem cells to BMP-2, thus forming a positive osteogenesis–angiogenesis feedback loop.[8,9] However, endogenous BMP-2 has shortcomings, such as a short half-life and low biological concentration. Moreover, the sustainable release of exogenous BMP-2 to maintain effective local concentrations and ensure its biological potency during initial repair is difficult to achieve. Accordingly, a BMP-2 gelatin/chitosan hydrogel sustained-release system was prepared via re-emulsification cross-linking, and effective bone defect repair was facilitated by its slow and continuous release.[10] Bone marrow mesenchymal stem cells (BMSCs) can be cultured, isolated, and expanded *in vitro* and have the potential for multidirectional differentiation. Additionally, BMSCs can transform into OBs under induction conditions. Consequently, BMSCs are considered to be ideal seed cells for tissue engineering and regenerative medicine owing to their wide range of sources, easy availability, strong multidirectional differentiation potential, low immunogenicity, and strong tissue repair ability.[11,12] Therefore, this study aimed to develop HA/ZrO_2 composites with satisfactory mechanical properties using SLA 3D-printing technology. The porosity and pore diameter of the materials were designed to overcome the abovementioned shortcomings. BMSCs were used as seed cells, and BMP-2 was used as an osteogenic inducer. The BMP-2 gelatin/chitosan hydrogel sustained-release system was prepared using the complex emulsion cross-linking method. After *in vitro* culture, the system was implanted into a 3D-printed gradient composite HA/ZrO_2 scaffold material to construct novel tissue-engineered bone. The engineered bone was then implanted into a rhesus macaque lumbar vertebral bone defect model. 16 weeks postoperatively, the osteogenic effect of the tissue-engineered bone in rhesus macaques was assessed by observing postoperative X-ray and microcomputed tomography (CT) images, performing hard-tissue sectioning and histological observation, and detecting the expression of osteogenic-related proteins (OGPs).

2. Materials and methods

2.1. Experimental animals and grouping

The experimental animals comprised 26 healthy rhesus macaque monkeys (14 male and 12 female, aged 4–6 years), each with a body weight of 6–10 kg (obtained from Kunming Animal Research Institute of the Chinese Academy of Sciences; Production License Number: SCXK(Dian)K2013-0005, Use License Number: SYXK(Dian)K2013-0012). The breeding operations were strictly carried out in accordance with the Breeding Requirements for Experimental Animals of the Kunming Animal Research Institute, Chinese Academy of Sciences. During the experiment, the 3R principles were followed to provide humane care and treatment of animals according to the Guiding Opinions on the Humane Treatment of Experimental Animals.

The 26 rhesus macaque monkeys were randomly assigned to four groups: tissue-engineered bone group A

(n = 10), which received the new gradient composite HA/ZrO_2 scaffold prepared via 3D printing, loaded with the BMP-2 gelatin/chitosan hydrogel sustained-release system and third-passage BMSCs2 (Rhesus monkeys (Macaca mulatta); blank material group B (n = 10), which received the blank gradient composite HA/ZrO_2 nanoscaffold; group C, the autologous iliac bone group (n = 4); and group D, the lumbar vertebral defect model group (n = 2).

2.2. Creation of lumbar vertebral defect model

Two rhesus macaque monkeys were selected to establish the lumbar vertebral defect model (n = 2). Anesthesia was induced via intramuscular injection of ketamine hydrochloride (Fujian Gutian Pharmaceutical Co., Ltd., Fujian, China (Batch No. 20161106). at a dose of 10 mg/kg, followed by intravenous anesthesia with pentobarbital sodium (Beijing Chemical Reagent Co., Ltd., Beijing, China (Batch No. 20160922) at a dose of 30 mg/kg. The rhesus macaque monkeys were secured in a right lateral recumbent position on the operating table, shaved, cleaned, and disinfected, and the surgical area was draped. An anterolateral approach was applied to the lumbar spine, and an oblique incision along the edge of the external oblique muscle from the lower end of the 12th rib downward to the midpoint of the pubic symphysis and navel was made, measuring 8–12 cm on the right side. The skin, subcutaneous tissue, and deep fascia were sequentially incised layer by layer. Hemostasis was achieved, and the lateral abdominal tendon was exposed and bluntly separated along the muscle fibers. The internal oblique muscle was incised, and the retroperitoneal space was bluntly dissected to expose the surgical segment (L4 or L5) of the vertebral body. The L4 vertebral body and the adjacent upper and lower vertebrae were exposed, and the accompanying lumbar arteries and veins were ligated. Thereafter, using the transverse process as a boundary, the anterior two-thirds of the vertebral body parallel to the coronal plane were completely chiseled off, and the upper and lower intervertebral discs and the cartilage endplates on both sides were scraped off to create a vertebral body defect model (Figure 1A–1B).

2.3. Fabrication of scaffolds, hydrogel system, and tissue-engineered bone

2.3.1. Photopolymerization 3D printing of ZrO_2 ceramics

The lumbar vertebral defect model was then scanned with micro-CT (SKYSCAN, Bruker Corporation, Belgium) to obtain plain images along with two-dimensional (2D) and 3D reconstruction images. The data were copied, and the resulting output was in DICOM format. The porosity of the composite scaffold material was set to 25 pores per inch, and the obtained STL format file was further processed. Finally, a hollow semicylindrical body with uniform pores and a pore diameter of approximately 500 μm that penetrated the inner and outer wall was obtained and exported in STL format. The obtained STL file was further

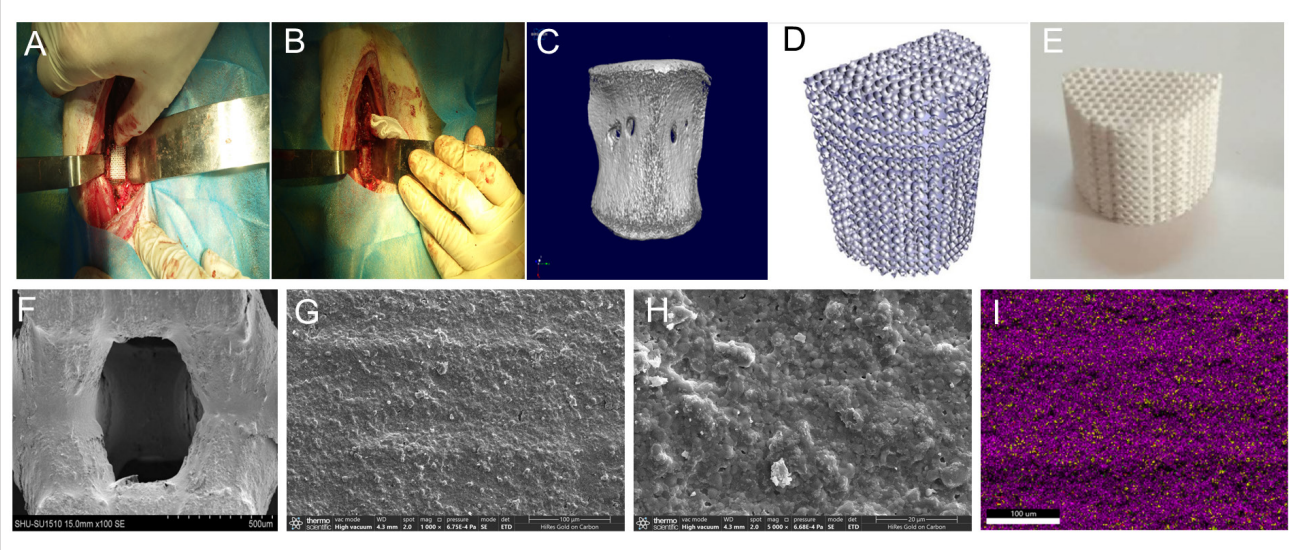

Figure 1. Preparation of tissue-engineered bone. (A,B) Establishment of the lumbar vertebral defect model and implantation of the tissue-engineered bone in animal experiments. (C) Placement of the excised L4 vertebral defect models into a microcomputed tomography system for plain scan imaging and 2D and 3D reconstructions. (D) 3D structure of the material formed after postprocessing the data. (E) HA/ZrO_2 gradient composite material prepared by photocuring and subsequent defatting and sintering. (F–H) Scanning electron microscope images of the HA/ZrO_2 gradient composite material. Scale bars: (F) 500 μm, (G) 100 μm, (H) 20 μm; magnifications: (F) 100×, (G) 1,000×, (H) 1,000×. (I) Elemental scanning analysis of hydroxyapatite/zirconia gradient composite materials.

processed and imported into a CeraFab 7500 photopolymer 3D printer. The planar resolution was set to 40 μm (635 dpi), pixel (X,Y) 1920 × 1080, stage size (X,Y,Z) 76 mm × 43 mm × 150 mm, layer thickness 25 μm, exposure time 1 s, and the initial printing layer thickness parameter was set to 10 μm. Nanograde ZrO_2 slurry was prepared, and photosensitive resin was added to achieve a ZrO_2-to-resin mass ratio of 15%, which was then poured into the material tank. The printing program was started according to the set parameters. The integrated UV-LED light source of the CeraFab 7500 (Lithoz GmbH, Vienna, Austria) induced a polymerization reaction in the resin, and the material solidified layer by layer to form a composite photosensitive resin preform. After the preform was formed, it underwent further debinding and sintering treatment, which was carried out simultaneously. The specific steps were as follows:

(i) Drying and evaporation stage: The temperature was increased from 25 to 75°C over 4 h, the heating rate was 0.208 K/min, and the holding time was 6 h to allow the excess water to evaporate. The temperature was then raised to 500°C with specific heating rates and holding times adjusted for each stage.

(ii) Degreasing and high-temperature sintering stage: From 500 to 1,250°C, the heating time was controlled at 7.5 h, the rate was 1.677 K/min, and no holding was required after the temperature reached 1,250°C. The temperature continued to rise to 1,450°C, with the heating rate set at 3.333 K/min, taking 1 h and holding for 2 h.

(iii) Cooling stage: After reaching the highest sintering temperature of 1,450°C, it was held for 2 h and then cooled at −0.660 K/min for 36 h to 25°C. The entire degreasing and sintering process lasted 120.5 h (Figure 1C–1E).

2.3.2. Preparation of HA/ZrO_2 gradient composite scaffolds (dip-coating method)

The HA/ZrO_2 gradient composite material was prepared via a dip-coating method. The slurry for the first layer consisted of 31.1% nanosized ZrO_2 powder (prepared by the School of Materials Science and Engineering, Shanghai University, Shanghai, China), 13.3% nanosized HA powder (prepared by the School of Materials Science and Engineering, Shanghai University, Shanghai, China), 53% double-distilled water, 1.4% ethyl phosphate (prepared by the School of Materials Science and Engineering, Shanghai University, Shanghai, China), and 0.2% ethyl cellulose (prepared by the School of Materials Science and Engineering, Shanghai University, Shanghai, China). HA was heated to 800°C and held for 2 h. The double-distilled water was heated to 50°C, and the above materials were mixed and added to the double-distilled water, stirring thoroughly. The photocured pure ZrO_2 ceramic was immersed in the slurry to ensure full penetration, then removed, and the excess slurry was discarded. It was dried in a 100°C electric furnace for 2 h, then heated to 900°C and held for 5 h, and finally heated to 1,250°C and held for 1 h. The second-layer slurry composition was 3.9% nanosized ZrO_2 powder, 35.5% nanosized HA powder, and 58% double-distilled water. The ratio of ethyl phosphate to ethyl cellulose remained unchanged. The above steps were repeated. After cooling, the HA/ZrO2 gradient composite material was obtained. The 3D-printed HA/ZrO_2 gradient composite scaffold material was placed on the sample stage and fixed with conductive adhesive. Thereafter, the 3D surface structure was observed, and elemental scans were performed using a scanning electron microscope (SU-1510, Hitachi, Tokyo, Japan) (Figure 1F–1I).

2.3.3. Preparation of gelatin microspheres and chitosan hydrogel system

One gram of gelatin powder (Shanghai Zhuojing Electronic Technology Co., Ltd., Shanghai, China) was weighed using an electronic balance (Sigma-Aldrich, St. Louis, MO) and dissolved in 10 mL of 50°C deionized water. Under magnetic stirring (500 rpm), the dissolved gelatin solution was added dropwise to 60 mL of preheated 50°C olive oil (Shanghai Nuochen Biotechnology Co., Ltd., Shanghai, China) under magnetic stirring (500 rpm; Shanghai Boxun Medical Biological Instrument Corp., Shanghai, China). Stirring was maintained to form a stable emulsion, and subsequently continued until the mixture gradually cooled to 4°C to form solid microspheres. The microspheres were rinsed three times each with acetone (Sinopharm Chemical Reagent Co., Ltd., Shanghai, China) and ethanol (Sinopharm Chemical Reagent Co., Ltd., Shanghai, China) at 4°C. Finally, the resulting microspheres were freeze-dried. An appropriate amount of ethanol solution containing 50 mM glyoxal (Sinopharm Chemical Reagent Co., Ltd., Shanghai, China) was taken, and the prepared gelatin microspheres were placed into the ethanol solution. The mixture was stirred at 25°C for 10 h and allowed to stand until the microspheres precipitated. The supernatant was discarded, and the microspheres were washed twice with ethanol, filtered, and freeze-dried.

To prepare the gelatin microsphere-encapsulated chitosan hydrogel, chitosan powder (Sigma-Aldrich, St. Louis, MO) was dissolved in aqueous acetic acid (Sinopharm Chemical Reagent Co., Ltd., Shanghai, China) to obtain a 1.5% (w/v) solution under sterile conditions. Separately, sodium β-glycerophosphate (Sinopharm Chemical Reagent Co., Ltd., Shanghai, China) was

dissolved in deionized water to obtain a 50% (w/v) solution, which was filtered and stored at 4°C. The dissolved BMP-2 (Sigma-Aldrich, St. Louis, MO) and the prepared gelatin microspheres were added to 50 mL of 1.5% (w/v) chitosan solution. The pH was adjusted to 6.3 using precision pH paper. A 50% (w/v) sodium β-glycerophosphate solution was added dropwise to the chitosan solution under magnetic stirring until the final solution contained 88 mM sodium β-glycerophosphate and had a pH of approximately 7.2. The resulting hydrogel was incubated at 37°C for 3 h. The specimen was then removed and fixed to a sample holder with cryo-glue (Sigma-Aldrich, St. Louis, MO). Scanning electron microscopy (SEM; SU-1510, Hitachi, Tokyo, Japan) was performed on the gelatin/chitosan microspheres and the gelatin/chitosan microsphere-encapsulated BMP-2 hydrogel to observe their surface morphology and internal structure (Figure 2A–2C).

2.3.4. Encapsulation efficiency, drug loading, and in vitro sustained-release evaluation

The amount of residual BMP-2 in the supernatant was detected using an enzyme-linked immunosorbent assay (ELISA) kit (Abcam, Cambridge, MA (Catalog No. ab11985) to infer the drug loading and encapsulation efficiency of the chitosan-encapsulated gelatin microsphere BMP-2 hydrogel. The absorbance (optical density [OD]) at A450 and calibrated A570 wavelengths was measured using a spectrophotometer (Beijing Persee General Instrument Co., Ltd., Beijing, China) according to the ELISA kit instructions. The BMP-2 concentration in the sample was calculated using the standard equation of the standard curve, thus determining the BMP-2 content in the washing supernatant and the sample. The relevant curves were plotted according to the relationship between BMP-2 concentration and OD values over time.

Three test tubes (5 mL each) were prepared, and 150 mg of BMP-2 gelatin/chitosan hydrogel was added to each tube. 2 mL of PBS (pH 7.2) were added to each, and the tubes were incubated in a 37°C water bath with shaking. At different time points (6, 16 h, 1 d, 2, 3, 6, 9, 12, and 15 d), 100 μL of supernatant from each test tube was taken, and BMP-2 was measured using an ELISA detection kit, following the abovementioned procedures. The average was calculated, and based on ELISA measurements, the

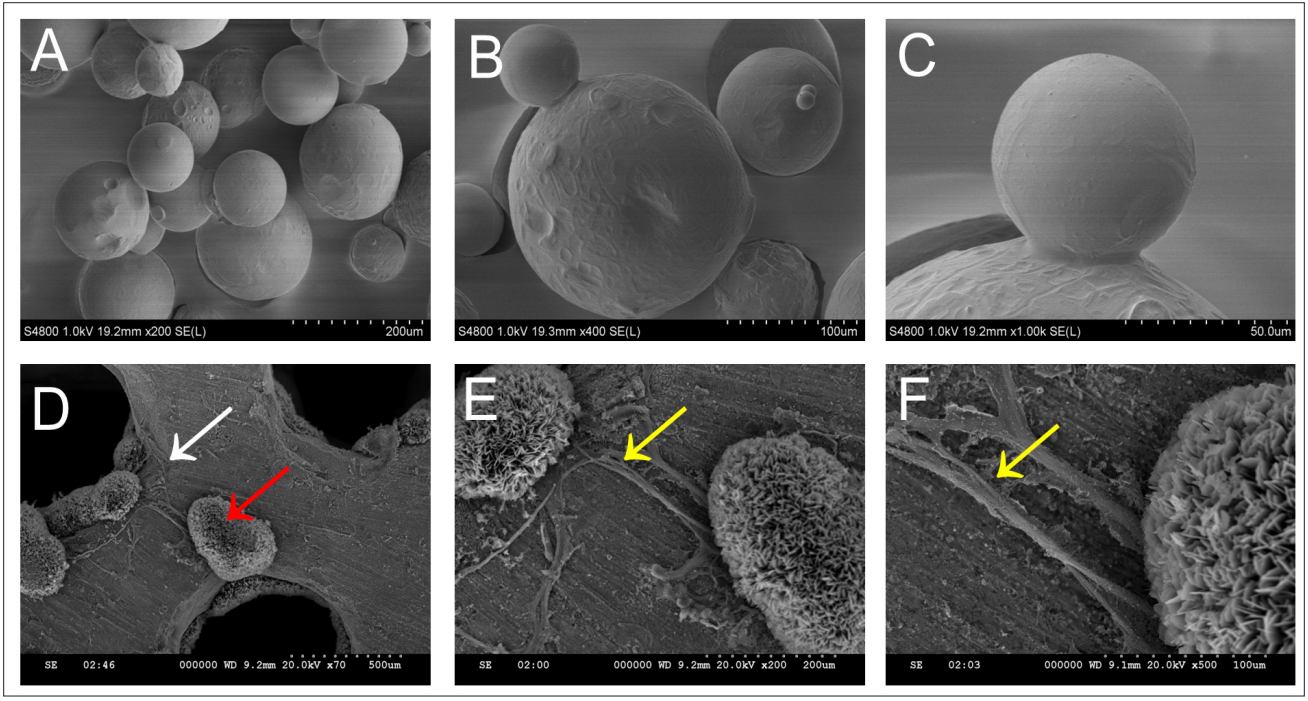

Figure 2. Morphological characterization of the gelatin/chitosan hydrogel system and the novel tissue-engineered bone. (A–C) Surface morphology of gelatin microspheres coated with chitosan hydrogel at different time points, observed by scanning electron microscope. Scale bars: (A) 200 μm, (B) 100 μm, (C) 50 μm; magnifications: (A) 200×, (B) 400×, (C) 1,000×. (D–F) Scanning electron microscopy images of the composite of HA/ZrO_2 gradient composite scaffold material, bone morphogenetic protein (BMP)-2 gelatin/chitosan sustained-release hydrogel system, and bone marrow mesenchymal stem cells (BMSCs). Scale bars: (D) 500 μm, (E) 200 μm, (F) 100 μm; magnifications: (D) 70×, (E) 200×, (F) 500×. The white arrow indicates the scaffold material, the yellow arrow indicates the BMSCs, and the red arrow indicates the BMP-2 gelatin/chitosan sustained-release hydrogel system. Both cells and hydrogel adhered to the nanoscaffold material, with favorable cell viability and morphology.

cumulative release curve of BMP-2 from the gelatin/chitosan hydrogel was plotted.

2.3.5. Construction of novel tissue-engineered bone

The prepared HA/ZrO_2 material was shaped into 5 mm × 5 mm × 5 mm cubic bodies. After high-temperature sterilization, the bodies were soaked overnight in a 0.01% (w/v) poly-L-lysine solution and then allowed to dry under aseptic conditions. The sterilized material was then placed in a culture dish and covered with culture medium. The prepared BMP-2 gelatin/chitosan hydrogel sustained-release system and third-passage BMSCs were made into a suspension and then slowly added dropwise to the cubic blocks of the composite scaffold material. The third-passage BMSCs were seeded on the material at a density of $5\times10^3/cm^2$. An induction solution (containing 100 nM dexamethasone, 50 mg/mL vitamin C, and 10 mM β-glycerophosphate) was added. The specimen was then cultured at 37°C for 48 h in a 5% CO_2 incubator. The culture medium and particles were washed away with PBS to obtain novel tissue-engineered bone. The specimen was removed, fixed to a sample holder with cryo-glue, and scanned by SEM to observe its surface morphology and internal structure (Figure 2D–2F).

2.3.6. Calculation of encapsulation efficiency and drug loading

The amount of remaining BMP-2 in the supernatant and the total amount of BMP-2 added were detected using ELISA. The drug loading and encapsulation efficiency of the gelatin/chitosan microsphere hydrogel encapsulating BMP-2 were then calculated using the following formulas:

(i) Drug loading efficiency calculation:

Drug loading efficiency = (Total amount of BMP-2 added - Amount of BMP-2 measured in the supernatant)/Total mass of microspheres × 100% (1)

(ii) Encapsulation efficiency calculation:

Encapsulation efficiency = (Total amount of BMP-2 added - Amount of BMP-2 measured in the supernatant)/Total amount of BMP-2 added × 100% (2)

2.4. Implantation procedures and postoperative animal management

All experimental animals were confirmed to have no lumbar deformities before surgery via X-ray. Following the established protocol, vertebral defect models were successfully created in 24 of the rhesus macaques. The tissue-engineered bone group (n = 10) was implanted with the new gradient composite HA/ZrO_2 tissue-engineered bone material prepared using 3D printing, which was loaded with the BMP-2 gelatin/chitosan hydrogel sustained-release system and passage 3 BMSCs. The blank material group (n = 10) was implanted with blank gradient composite HA/ZrO_2 nanoscaffold material, and the autologous iliac bone group (n = 4) was implanted with autologous iliac bone. During the surgery, X-ray positioning was used to confirm satisfactory implant placement, followed by fixation with a specially made contact steel plate of appropriate length (75 mm). The surgical site was thoroughly irrigated with saline, and after ensuring no instruments or gauze were left behind, the incision was closed layer by layer. Postoperatively, the experimental rhesus macaque monkeys were housed individually, with daily cleaning and disinfection of the wound, and were administered penicillin sodium (1.6 million U; (North China Pharmaceutical Co., Ltd., Shijiazhuang, China) intramuscularly once daily for 3 d to prevent infection.

2.5. Postoperative gross observation and X-ray imaging

The basic conditions of the rhesus macaque monkeys, such as activity and food intake, were checked daily. Any redness, swelling, discharge, abscess, infection, or ulceration at the surgical incision was recorded, and the walking activity of the lower limbs was noted.

At 8 and 16 weeks postoperatively, animals in each experimental group were anesthetized via intramuscular injection of ketamine hydrochloride (10 mg/kg). Anteroposterior and lateral radiographs of the lumbar spine were then taken using an X-ray device (HF100HA, Mikasa X-Ray, Japan) for each group to assess integration with the host bone and to observe whether the implanted biomaterials showed any fractures, degradation, or callus growth around the material. At 16 weeks, gross specimens were collected by euthanizing the animals via intramuscular injection of ketamine hydrochloride combined with bloodletting, followed by careful dissection to expose the experimental lumbar segments of the rhesus macaque monkeys. The fixation steel plates and screws were removed, and the surrounding soft tissues were rinsed and cleaned. The condition of the implanted biomaterials and the surrounding bone in the removed specimens was then evaluated.

2.6. Biomechanical testing and hard-tissue sectioning

Twelve animals (four per group) were euthanized with a ketamine and potassium chloride overdose at 16 weeks postsurgery to harvest bone samples. All residual musculature was carefully removed from the specimens to preserve all ligamentous structures. The specimens were trimmed, creating two parallel planes, and fixed on a testing machine (MTS 858, MiniBionix) along a plane that

was parallel to the long axis of the implants. Compression testing was performed at a speed of 20 mm/min, and the load was increased from zero until the specimens were destroyed. The maximal load, energy to maximal load, stiffness, and maximum compressive strength were then recorded.

After the bone tissue samples were collected, they were fixed with 10% neutral formalin (a volume 20 times that of the tissue; (Kunming Chemical Reagent Co., Ltd., Kunming, China) for 48 h, followed by tissue dehydration with a gradient of 70%, 80%, 85%, 90%, 95%, 100%, and 100% alcohol for 3 h each. Next, the samples were treated with xylene I (Sinopharm Chemical Reagent Co., Ltd., Shanghai, China) for 3 h, xylene II (Sinopharm Chemical Reagent Co., Ltd., Shanghai, China) for 3 h, methyl methacrylate infiltration solution I (Sinopharm Chemical Reagent Co., Ltd., Shanghai, China) for 3 d, and infiltration solution II (Sinopharm Chemical Reagent Co., Ltd., Shanghai, China) for 5 d. They were then embedded into a gel to form a resin block. Slow saw cutting was used to create 300-μm thick slices for sticking and grinding using a EXAKT 310 CP (EXAKT Technologies, Inc., Oklahoma City, OK). The slices were then ground to below 50-μm thickness and polished until scratch-free. Transverse and sagittal sections were then used to evaluate the formation of new bone.

2.7. Microcomputed tomography analysis and histological evaluation

At 8 and 16 weeks postsurgery, four animals (n = 2 from both groups A and B) were sacrificed as described previously to evaluate new bone formation via micro-CT (SkyScan, Bruker micro-CT, Belgium). Soft tissue was removed from the surface of the specimens from each rhesus macaque monkey. The specimens were then removed, wrapped, and fixed with plastic wrap, and then scanned using micro-CT under the following conditions: 80 kV, 80 μA, 2,000 ms, frame averaging of 4, and a pixel combination of 1 × 1. A 180° X-ray scan was used to locate the entire material area as the region of interest, and the CT signal selection function was used to suppress the ultrahigh signal area of the material itself to form a 2D image of the new bone. Micro-CT was then used to calculate the amount of new bone (bone volume [BV]) in the material area. Considering the different lengths of the modeled bone in each group, the amount of new bone per unit area was calculated according to this ratio. The built-in Microview ABA analysis software CTAn (CT Analyser), developed by Bruker, Kontich, Belgium was used for BV analysis.

Following micro-CT observation, the specimens were dehydrated with 70%, 80%, 95%, and 100% alcohol in a gradient manner, made transparent with xylene, and then infiltrated with a resin gradient. They were then embedded and solidified into embedding blocks. The embedding blocks were initially trimmed to the corresponding position using the EXAKT cutting and grinding system (EXAKT Apparatus GmbH & Co., Germany). Subsequently, the tissue within the embedding blocks was ground to the maximum surface using a grinding blade and adhered to a slide. The side with the adhered slide was cut to approximately 200 μm thickness, and the sections were further ground to a thickness of 50 μm on an EXAKT microgrinder, polished to a traceless finish, and subjected to hematoxylin and eosin (HE), toluidine blue, and immunofluorescence staining. The stained sections were observed under an optical microscope. HE staining showed cytoplasm and connective tissue as red or purple-red and nuclei as blue, while toluidine blue staining revealed bone cell nuclei in blue, cartilage in purple, osteoid in light blue, newly mineralized bone in dark blue, and mature bone in light blue.

2.7.1. Section treatment and antigen retrieval

The sections were soaked sequentially in xylene I for 15 min, xylene II for 15 min, anhydrous ethanol I for 5 min, anhydrous ethanol II for 5 min, 85% alcohol for 5 min, and 75% alcohol for 5 min, and then rinsed in distilled water. The tissue sections were then placed in a retrieval box filled with ethylenediaminetetraacetic acid antigen retrieval buffer (pH 8.0). Antigen retrieval was performed in a microwave oven at medium heat for 8 min; heating was then halted for 8 min before switching to medium-low heat for 7 min, which prevented excessive evaporation of the buffer and dehydration of the sections. After cooling naturally, the slides were soaked in phosphate-buffered saline (PBS; pH 7.4) and then shaken and washed on a decolorizing shaker three times for 5 min each.

2.7.2. Autofluorescence quenching and serum blocking

After lightly shaking off the sections, a circle was drawn around the tissue with a histology pen to prevent antibody diffusion. Autofluorescence quencher was then added to the circle for 5 min and rinsed with running water for 10 min. For serum blocking, bovine serum albumin was added to the circle and incubated for 30 min.

The blocking solution was gently shaken off, and the primary antibody diluted in PBS was added to the sections. The slides were then placed flat in a humid box and incubated at 4°C overnight. The slides were then soaked in PBS (pH 7.4), shaken, and washed on a decolorizing shaker three times for 5 min each. After gently shaking off excess liquid, the secondary antibody corresponding to the primary antibody was added to cover the tissue, followed by a 50-min incubation at approximately 24°C in the dark.

2.7.3. Nuclear staining and mounting

The slides in PBS (pH 7.4) were shaken and washed on a decolorizing shaker three times for 5 min each. After gently shaking off excess liquid, 4',6-diamidino-2-phenylindole (DAPI) staining solution was added to the circle and incubated at approximately 24°C in the dark for 10 min. For mounting, the slides in PBS (pH 7.4) were shaken and washed on a decolorizing shaker three times for 5 min each. After gently shaking off excess liquid, the slides were mounted with an antifluorescence quenching mounting medium.

2.7.4. Microscopy and image acquisition

Images were observed and collected using a fluorescence microscope. The DAPI ultraviolet excitation wavelength was 330–380 nm, the emission wavelength was 420 nm, and it emitted blue light. The fluorescein excitation wavelength was 465–495 nm, the emission wavelength was 515–555 nm, and it emitted green light. The Cyanine3 excitation wavelength was 510–560 nm, the emission wavelength was 590 nm, and it emitted red light.

2.8. Postoperative osteogenic protein analysis

16 weeks postoperatively, two rhesus macaque monkeys from each of the lumbar tissue-engineered bone group, the blank material group, and the autologous iliac bone group were selected. The animals were euthanized under anesthesia via intramuscular injection of ketamine hydrochloride combined with bloodletting. Under sterile conditions, the surgical segment of the vertebrae was removed, and the implanted materials were separated and cut into pieces. They were then placed in a tube containing lysis solution. Reverse transcription polymerase chain reaction (RT-PCR) and western blot analysis of alkaline phosphatase (ALP), osteocalcin (OCN), osteoprotegerin (OPG), VEGF, basic fibroblast growth factor (bFGF), osteopontin (OPN), and type I collagen were then performed.

2.9. Statistical analysis

Data were analyzed using SPSS 22.0 software (SPSS Inc., USA), and the results are presented as the mean ± standard deviation, with statistical significance set at $p < 0.05$. Differences between the experimental groups were compared and validated via one-way analysis of variance using the Fisher protected least significant difference method.

3. Results

3.1. Morphological characteristics of the novel tissue-engineered bone

The drug loading and encapsulation efficiency of BMP-2 in gelatin/chitosan microsphere hydrogels at different time points were calculated using the above formulas: In the first 2 d, both drug loading and encapsulation efficiency remained at relatively high levels (62.1% and 53.5%, respectively). Starting from Day 3, they decreased rapidly, reaching 36.3% ± 0.7% and 54.5% ± 0.5% by Day 6. From Days 6 to 12, the decline slowed, with drug loading and encapsulation efficiency decreasing to 36.3% ± 0.7% and 45.9%±0.7% by Day 12. From Days 12 to 15, these parameters entered a stable phase, and by Day 15, drug loading and encapsulation efficiency remained above 30% and 45%, respectively (Table 1). The drug loading and encapsulation efficiency profiles over time are illustrated in Figure 3A.

The A450 and calibrated A570 wavelength absorbance (OD) values were determined according to the ELISA method. The concentration and OD value of BMP-2 gradually increased over time, rising slowly on the first day, and reaching 627.62 ± 5.41 (pg/mL) and 0.365 ± 0.004, respectively. From Days 2 to 6, they increased rapidly, reaching 2274.76 ± 10.91 (pg/mL) and 1.518 ± 0.008 on Day 6. After Day 6, they continued to increase slowly, reaching 3021±12.9 (pg/mL) and 2.042±0.009 on Day 15 (Table 2). A corresponding curve illustrating the relationship between BMP-2 concentration and OD values over time was then plotted (Figure 3B–3C).

The recombinant protein BMP-2 exhibited a phased release pattern. Within the first 24 h, the release rate was slow, corresponding to the adaptation phase. From Days 1 to 6, BMP-2 showed a burst release phase, with the cumulative release rate reaching 45.5% ± 0.25% on Day 6. Thereafter, it gradually entered a slow-release phase (Days 6–12), with the cumulative release rate reaching 54.1% ± 0.5% on Day 12, and finally entered a stable phase (Days 12–15), with the BMP-2 release rate at 55% ± 0.16% on Day 15. The BMP-2 concentration in the samples was calculated according to the standard curve formula, thereby determining the BMP-2 content in the washing supernatant and the samples and plotting the BMP-2 release curve and the standard curve (Figure 3D–3E).

Table 1. Bone morphogenetic protein-2 drug loading and encapsulation efficiency.

Time	6 h	16 h	1 d	2 d	3 d	6 d	9 d	12 d	15 d
Drug loading (%)	62.1 ± 0.9	59.4 ± 0.8	58.2 ± 0.5	53.5 ± 0.9	43.4 ± 0.6	36.3 ± 0.7	33.3 ± 0.8	30.6 ± 0.5	30.1 ± 0.4
Encapsulation efficiency (%)	93.7 ± 0.8	89.1 ± 0.5	87.4 ± 0.9	80.3 ± 1.0	65.1 ± 0.9	54.5 ± 0.5	50.0 ± 0.9	45.9 ± 0.7	45.2 ± 0.6

Abbreviations: d, Day; h, Hour.

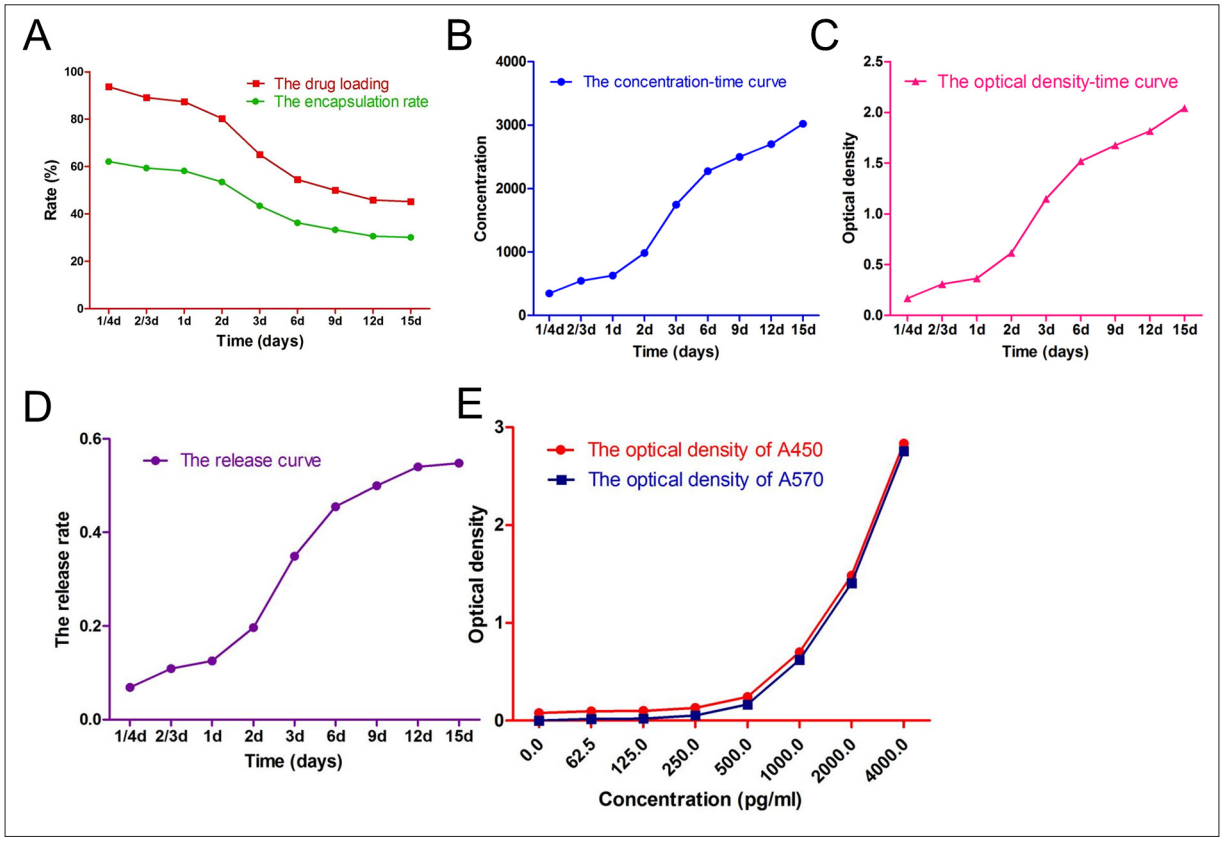

Figure 3. Drug loading, encapsulation efficiency, and *in vitro* release kinetics of the BMP-2 gelatin/chitosan hydrogel system. (A) Drug loading and encapsulation efficiency of the gelatin/chitosan sustained-release hydrogel loaded with bone morphogenetic protein (BMP)-2 at different time points. (B,C) Concentration–time curve and optical density–time curve for BMP-2. (D,E) Cumulative release curve of BMP-2 from the gelatin/chitosan sustained-release hydrogel and the standard curve of BMP-2.

Table 2. Bone morphogenetic protein-2 concentration and OD value.

Time	6 h	16 h	1 d	2 d	3 d	6 d	9 d	12 d	15 d
Concentration (pg/mL)	346.19 ± 0.82	545.24 ± 0.82	627.62 ± 5.41	983.81 ± 11.89	1745.24 ± 25.65	2274.76 ± 10.91	2498.1 ± 16.5	2700.5 ± 29.3	3021 ± 12.9
OD Value	0.168 ± 0.001	0.308 ± 0.001	0.365 ± 0.004	0.615 ± 0.008	1.148 ± 0.018	1.518 ± 0.008	1.675 ± 0.012	1.816 ± 00.021	2.042 ± 0.009

Abbreviations: d, Day; h, Hour; OD, Optical density.

Scanning electron microscopy observations at various magnifications revealed that the HA/ZrO_2 gradient composite scaffold material had a smooth surface and uniform structure. The fracture surfaces were tightly bonded to each other without distinct boundaries, and the uniform porosity of the material could provide a framework and channels for the ingrowth of new bone tissue, effectively ensuring uniform stress distribution in the composite scaffold material. The scaffold material possessed a 3D reticular structure, with chitosan microspheres evenly distributed on the material surface and within the pores. The material surface was uniformly coated with BMSCs, with cells adhering and dispersing without forming clumps. The gelatin/chitosan sustained-release hydrogel containing BMP-2 and BMSCs was evenly encapsulated on the material and within the pores.

3.2. Lumbar defect repair effects and histological analysis

All experimental rhesus macaques survived and remained healthy until the end of the experiment and were able to stand, walk, and eat independently after surgery. However, their appetite decreased owing to postoperative pain. Defecation and urination remained normal, and the monkeys demonstrated good activity levels and responsiveness to the external environment. 2

weeks postoperatively, all experimental rhesus macaques showed primary healing of the incision with good soft tissue coverage. 1 month postoperatively, the limbs of the experimental rhesus macaques moved freely.

Immediately after the operation, X-ray imaging in anteroposterior and lateral views of the lumbar spine showed that the lumbar bone defect model was well-established, the scaffold material was implanted, and the internal fixation in the lumbar group was satisfactory. 8 weeks postoperatively, the scaffold materials in groups A and B were not displaced or fractured; no spinal deformity was observed at the surgical segment, the bone defect ends were absorbed, and callus formation gradually increased, which was more pronounced in group A. In the autologous bone group, there was continuous callus formation between the implanted bone ends and the bone defect ends. 16 weeks postoperatively, X-ray images showed that the scaffold material in group A was slightly degraded, the material density was comparable with that of the host bone, and the surrounding new bone was closely connected to the host bone. In group B, the scaffold material was partially degraded, the density was lower than before, the gap between the scaffold material and the break ends was gradually filled with new bone, and the boundary was more blurred than before. In the autologous bone group, the implanted bone and the host bone cut line disappeared, and the two had completely fused (Figure 4).

Immediate postoperative imaging revealed well-formed lumbar spinal bone defect models, with satisfactory implant positioning and internal fixation. 8 weeks postoperatively, the density of the scaffold materials in groups A and B was slightly reduced, with no displacement or protrusion of the material, no spinal deformity at the surgical segment, and no protrusion or fracture of the internal fixation within the lumbar group (Figure 4A–4B). Moreover, the boundaries between the biomaterials and the fracture ends were slightly blurred, with external callus formation at the bone defect ends, which was more pronounced in group A (Figure 4A–4B). In the autologous iliac bone group, obvious bone hyperplasia and external callus formation were observed at the osteotomy site, with the boundary between the implanted bone and the defect site becoming blurred and continuous callus bridging the defect (Figure 4C). 16 weeks postoperatively, in group A, the material was gradually degraded, surrounded by new bone callus, and the density of the transplanted material was close to that of the host bone (Figure 4A). Furthermore, the boundary and internal structure of the bone defect were blurred, with ground-glass opacity indicating new bone formation inside, and the boundary between the biomaterial and the fracture end disappeared (Figure 4A). In group B, the density of the scaffold material was reduced, and the material was partially degraded, with callus formation at the bone defect end (Figure 4B). In addition, the boundary between the biomaterial and the fracture end was more blurred (Figure 4B). In the autologous bone group, the transplanted bone and the host bone completely fused, and the osteotomy line disappeared (Figure 4C).

16 weeks postoperatively, eight animals were euthanized (four each from groups A and B). Macroscopic examination showed that the scaffold materials were well integrated with the host bone. In group A, substantial new bone tissue covered and enveloped the internal fixation, with new bone callus growing into the internal pores of the material, thereby demonstrating continuity. In addition, some material degradation was observed, with the newly formed bone tightly connected to the remaining scaffold material. In group B, the amount of new bone was less than that in group A, the connection between the scaffold material and the host bone was sparser, and some parts of the scaffold material remained exposed (Figure 5A). The specimens were placed in the micro-CT for scanning, reconstruction, and calculation of the total amount of new bone in each group. In group A, partial degradation of the scaffold material was observed during 3D scanning, with material density higher than that of the host bone. Moreover, trabecular bone formed inside the material, with a large amount of new bone formation at the contact end between the material and the host bone, and the two were tightly connected. In group B, partial degradation of the material was observed, with new bone growing into the material; however, this was considerably less than that in group A, and the connection between the two was looser (Figure 5B). According to the Microview ABA software analysis results, the BV in group A was consistently higher than that in group B (Table 3).

Hard-tissue sectioning was performed on the excised specimens. The hard-tissue sections showed that both the tissue-engineered bone group and the blank material group achieved integration between the scaffold material and the host bone. The tissue-engineered bone group exhibited a large amount of new bone tissue that had grown into the internal pores of the material, thereby showing continuity. Moreover, some material degradation was observed, with the newly formed bone tightly connected to the undegraded material. In contrast, the blank material group had less new bone, and the connection between the scaffold material and the host bone was sparser, indicating that the tissue-engineered bone group had better osteogenic efficacy than the blank material group (Figure 5C).

12 animals (n = 4 per experimental group) were euthanized 16 weeks after surgery to harvest bone samples

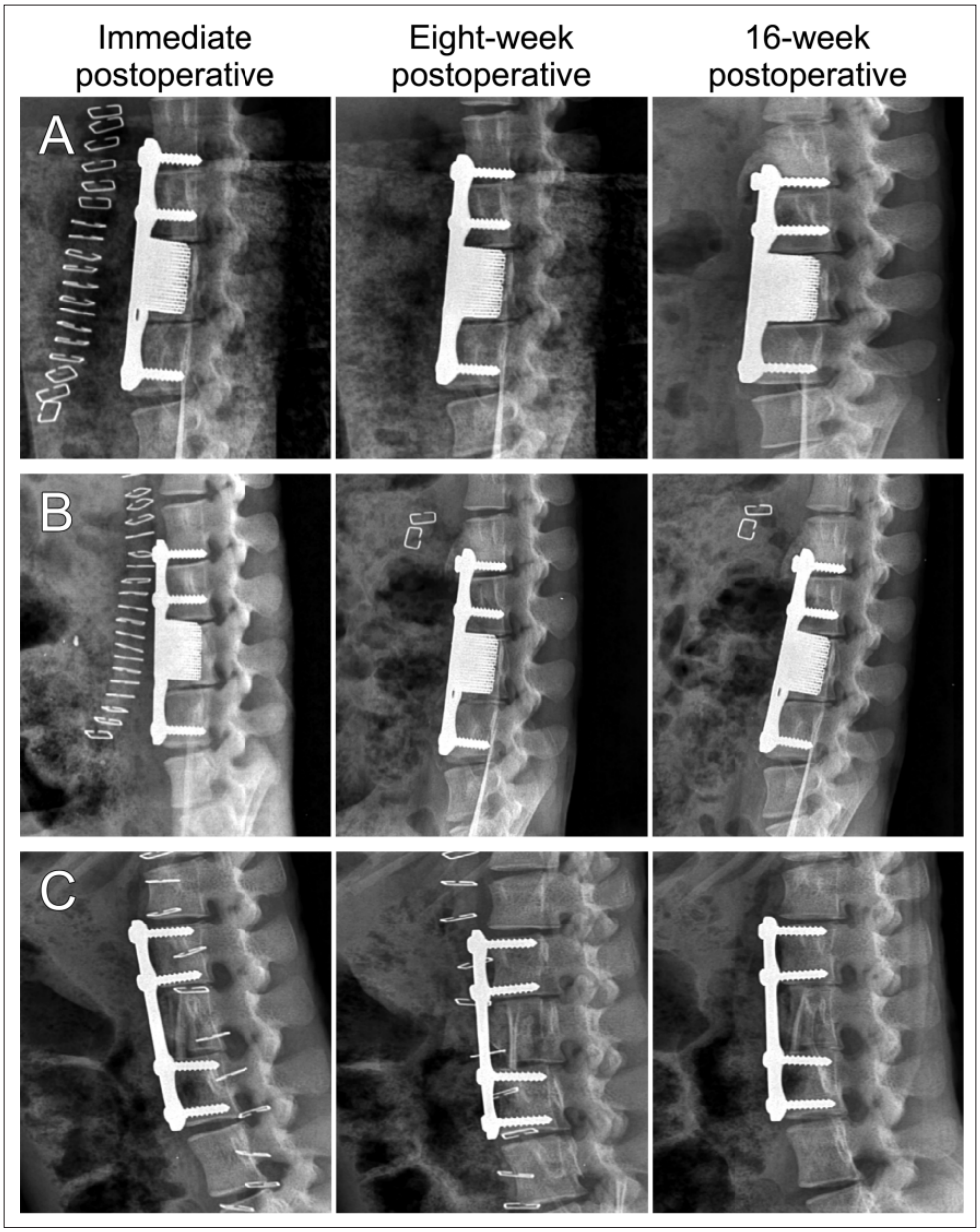

Figure 4. X-ray results. (A–C) Immediately postoperative, 8-week postoperative, and 16-week postoperative lumbar X-ray results for groups A, B, and C, respectively.

for biomechanical testing. The maximal load, stiffness, and maximal pressure in group B were significantly lower than those of the other two experimental groups and the nonoperated healthy group ($p < 0.05$), whereas the energy to maximal load in groups A and C was significantly higher than that in group B ($p < 0.05$) (Table 4).

Specimens were subjected to HE and toluidine blue staining as well as immunofluorescence processing. Both groups showed new trabecular bone that gradually crept into the pores of the scaffold material and increased in mass over time. 16 weeks postoperatively, at the connection between the implanted material and the host bone in group A, new lamellar bone was interwoven and fused with the host bone. Inward observations revealed that the new bone plate longitudinal ligament was surrounded by new woven bone, with elongated vertical grooves in the lamellar bone, which contained microvessels and osteogenic-related cells. Inside the pores of the implanted material, new bone tissue was distributed in a trabecular-woven bone pattern, with denser osteogenic-related cells visible within the trabecular

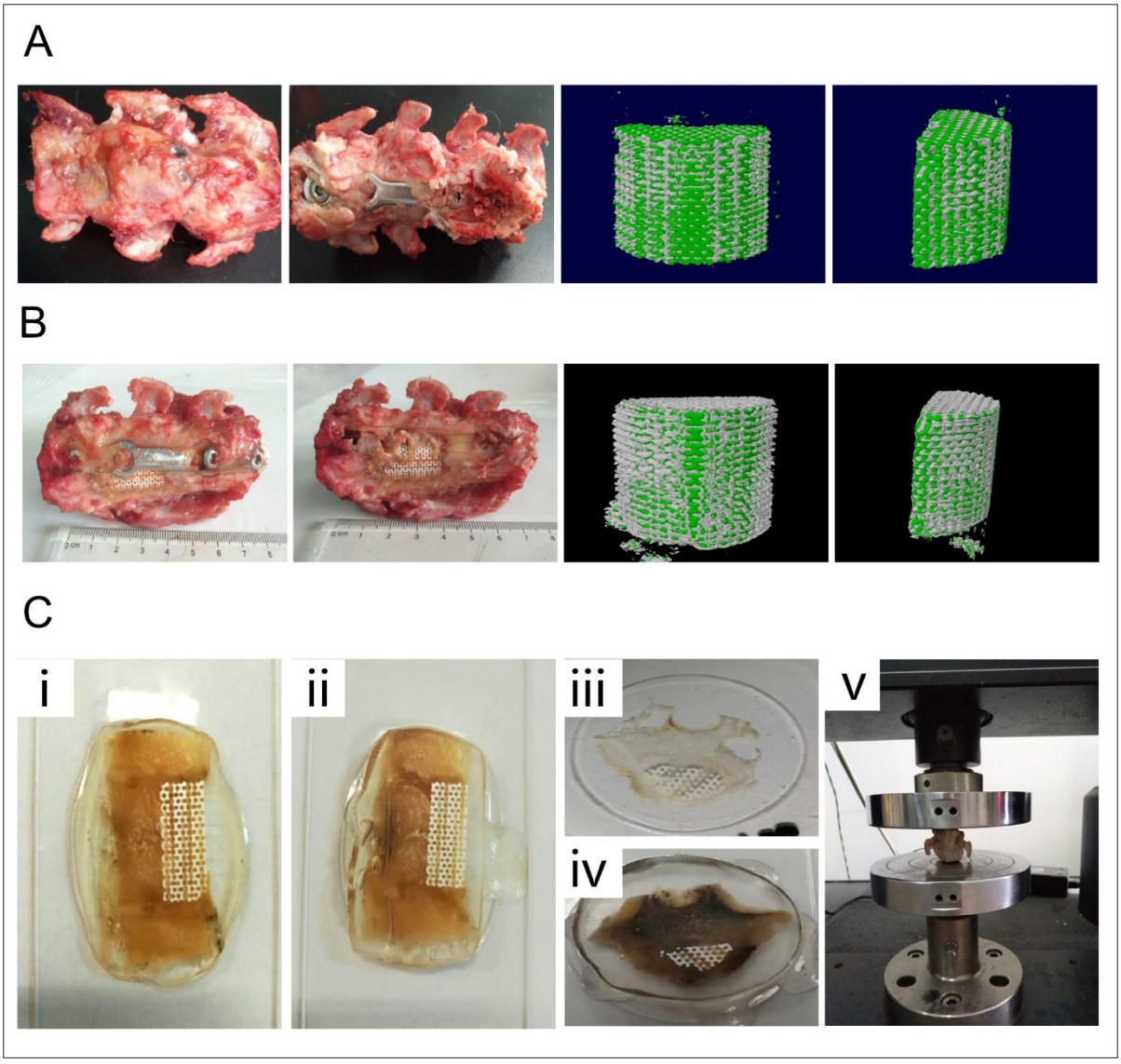

Figure 5. Evaluation of osteogenic efficacy and scaffold integration in rhesus macaques at 16 weeks postimplantation. (A,B) Macroscopic appearance and 3D microcomputed tomography (CT) images of specimens from groups A and B 16 weeks postoperatively. In group A, the scaffold material is completely covered by new bone tissue, with callus enveloping the internal fixation. In contrast, group B shows less callus formation, with parts of the scaffold material remaining exposed. In the micro-CT images, white represents the scaffold material and green represents new bone tissue; group A demonstrates significantly more new bone formation than group B. (C [i–ii]) Sagittal section of the hard-tissue slices of specimens from groups A and B 16 weeks postoperatively. (C [iii–iv]) Transverse sections of hard-tissue slices of specimens from groups A and B 16 weeks postoperatively. In the sagittal view, the scaffold materials of both groups are tightly connected to the host bone, with group A showing more yellow-brown bone tissue growing into the scaffold pores than group B. In the transverse view, new bone envelopes the scaffold material in both groups, with more degradation of the scaffold material in group A than in group B. (C [v]) Trimmed specimens from each group subjected to biomechanical testing.

Table 3. Microcomputed tomography new bone volume (BV) in the defect region.

Group	BV (mm^3), individual values			BV (mm3), mean ± standard deviation
Lumbar spine A (n = 3)	467.89	476.46	498.25	487.33 ± 11.62
Lumbar spine B (n = 3)	372.14	365.27	388.46	375.38 ± 10.51

Table 4. Biomechanical results at 16 weeks postoperative.

Item	Group A	Group B	Group C
Maximal load (N)	2,525.3 ± 298.8	1,373.5 ± 101.6*	2,920.6 ± 282.8
Maximal pressure (MPa)	3.2 ± 1.0	2.4 ± 0.7*	3.8 ± 1.1
Stiffness (N/mm)	1,779.5 ± 177.6	1,130.4 ± 119.4*	1,988.6 ± 221.7
Energy to maximal load (J)	3.2 ± 0.4	1.4 ± 0.2	7.1 ± 1.3*

Notes: Results are expressed as mean ± standard deviation. An asterisk (*) indicates a statistically significant difference compared with the normal group.

pores. In group B, partial degradation of the biomaterial was observed, with fewer newly formed trabecular bones that did not form an interconnected pattern with the scaffold, leaving clear gaps between them (Figure 6). Immunofluorescence showed OPG in red within the cytoplasm and nuclei in blue. The expression levels of ALP, OCN, OPG, VEGF, bFGF, OPN, and type I collagen were higher in group A than in group B (Figure 7).

3.3 Expression analysis of osteogenic proteins

16 weeks postoperatively, four animals were euthanized (two each from groups A and B). The expression of ALP, OCN, OPG, VEGF, bFGF, OPN, and type I collagen was detected using RT-PCR and western blotting. RT-PCR revealed that gene expression levels in group A were significantly higher than those in group B (Figure 8A). The western blot results were consistent with the RT-PCR findings, indicating that the expression levels of OGPs in

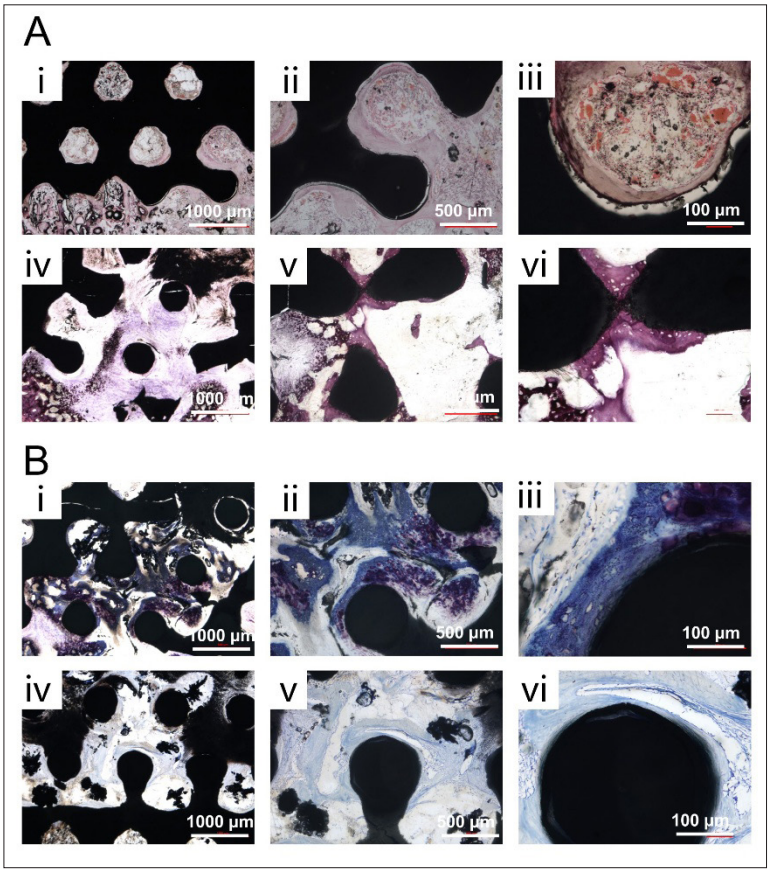

Figure 6. Hematoxylin and eosin (HE) and toluidine blue staining of groups A and B. (A-i–ii, A-iii–iv, A-v–vi) HE staining at different magnifications shows new bone callus infiltrating the scaffold pores, along with partial scaffold degradation. (B-i–ii, B-iii–iv, B-v–vi) Toluidine blue staining of groups A and B at different magnifications: purple areas (red arrows) indicate new cartilage, light blue areas (yellow arrows) denote osteoid, and lighter blue areas (white arrows) correspond to mature bone. Scale bars: B-i (1000 μm) B-ii (500 μm) B-iii (100 μm) B-iv (1000 μm) B-v (500 μm) B-vi (100 μm). Both HE and toluidine blue staining reveal more extensive and continuous bone callus formation in group A compared with group B, where scaffold pores remain incompletely filled by new bone tissue.

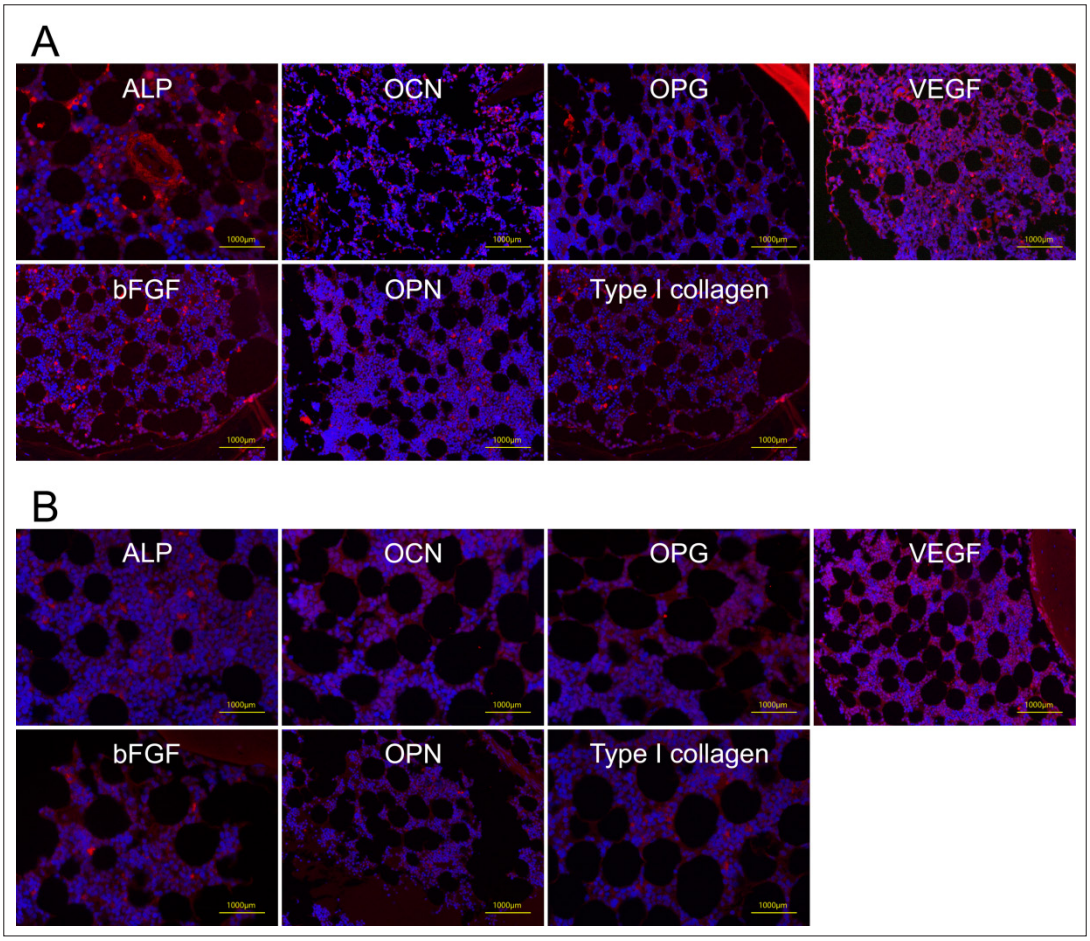

Figure 7. Immunofluorescence of osteogenic-related proteins (OGPs) (A,B). Immunofluorescence of alkaline phosphatase (ALP), osteocalcin (OCN), osteoprotegerin (OPG), vascular endothelial growth factor (VEGF), basic fibroblast growth factor (bFGF), osteopontin (OPN), and type I collagen in specimens from groups A and B 16 weeks postoperatively. Expression levels in group A were higher than those in group B.

group A were higher than those in group B (Figure 8B; raw western blot images are shown in Figure S1).

4. Discussion

In this study, a novel bone scaffold material was designed and prepared. The material consisted of a porous gradient HA/ZrO_2 composite and a gelatin/chitosan sustained-release hydrogel. The HA/ZrO_2 composite was prepared using SLA 3D-printing technology, and the hydrogel contained BMP-2 and BMSCs. Ultimately, the scaffold material was used to repair lumbar vertebral bone defects in rhesus macaques, and its efficacy in bone defect repair was evaluated. With the rapid development of 3D printing in the medical field, light-curing SLA printing technology has been increasingly applied in the preparation of biomedical materials.[13,14] SLA printing technology adjusts the porosity (70%–90%), pore size (100–500 μm), and connectivity of the material according to the different characteristics of the bone defect site. This allows for the preparation of personalized scaffold material that matches the morphology of the bone defect.[15] Personalized design of scaffolds, including porous structures, nanoscale channels, and gradient material distributions, helps promote cell growth, vascularization, and bone regeneration. The porous structure is designed to provide sufficient surface area for cell attachment and proliferation, while its internal structure mimics the microscopic environment of native bone tissue. This promotes osteogenic development and mineralization and provides a framework for the differentiation, expansion, and migration of OBs, chondrocytes, and vascular endothelial cells.[16] Additionally, this 3D interconnected structure facilitates the transport of nutrients and metabolites and provides a site for the continuous deposition and accumulation of extracellular matrix.[17] Moreover, the scaffold material exhibits excellent biocompatibility, and the porous

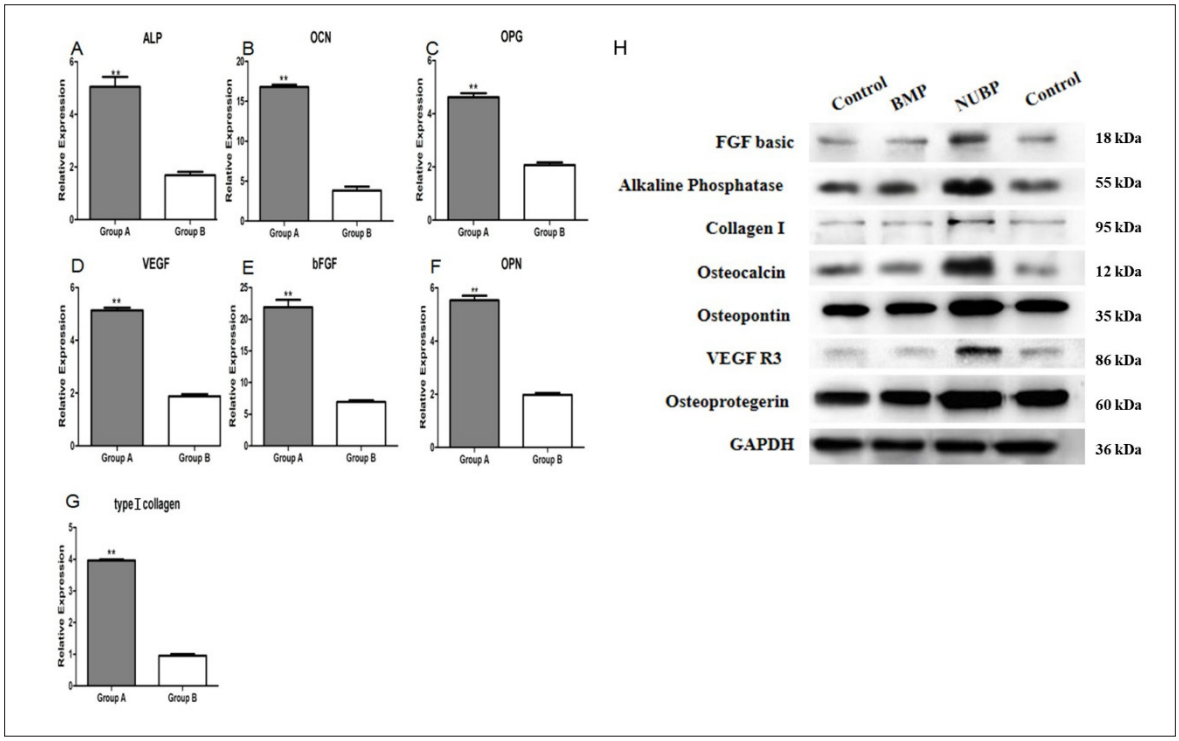

Figure 8. Reverse transcription polymerase chain reaction (RT-PCR) and immunoblotting analysis of osteogenic-related genes and proteins (OPGs). (A) RT-PCR results for alkaline phosphatase (ALP), osteocalcin (OCN), osteoprotegerin (OPG), vascular endothelial growth factor (VEGF), basic fibroblast growth factor (bFGF), osteopontin (OPN), and type I collagen in groups A and B. Gene expression levels in group A were significantly higher than those in group B. (B) Immunoblotting analysis showing higher expression levels of OPGs in group A than in group B. Raw western blot images are available in **Figure S1**.

structure markedly increases the surface area of the connection between the graft material and the new bone, which allows the material to form a strong connection to the host bone.[18] Histological analysis showed that over time after surgery, the trabeculae and amount of new bone in the composite scaffold material gradually increased, and the progressive formation of new bone and its reconstruction in the scaffold pores were clearly evident. Postoperative micro-CT scans revealed that the internal pores of the composite scaffold maintained a cross-linked 3D structure, which was covered internally by new bone tissue components. Some of these components were degraded and replaced by new bone, while undegraded material was tightly wrapped by newly formed trabecular bone, creating a cross-linked and integrated structure. Bone regeneration relies not only on intramembranous and endochondral ossification but also on the synergistic effects of angiogenesis and neurogenesis. Toluidine blue staining showed new cartilage in purple, osteoid in light blue, newly mineralized bone in dark blue, and mature bone in light blue, suggesting that bone formation within the scaffold was related to both endochondral and intramembranous osteogenesis.[19] Zirconia, being an inert material, possesses strong mechanical properties and low toxicity. It is nondegradable after implantation and does not accumulate in body tissues, muscles, or bones.[20,21] In this study, the use of zirconia resulted in a scaffold material with reliable mechanical strength and good mechanical properties. The mechanical testing showed that the mechanical strength and elastic modulus of the scaffold material group were higher than those of the blank group. As this study primarily focused on *in vivo* osteogenesis and biomechanical outcomes, the specific mechanical parameters of the scaffolds before implantation were not quantified. However, the rigorous sintering process at 1,450°C ensures the densification and intrinsic mechanical stability of the zirconia matrix. Moreover, the high compressive strength observed 16 weeks postimplantation provides strong indirect evidence that the initial scaffolds possessed sufficient load-bearing capacity to support spinal stability during the critical early healing phase. Hence, the material could be used for implantation in load-bearing areas of the body.

Osteoblasts can secrete osteogenic proteins, such as ALP, type I collagen, and OCN. In the matrix secreted by

OBs, the main structural component is type I collagen, and the amorphous components are OPN, OCN, and various growth factors, such as bFGF and VEGF.[22,23] Type I collagen, an early marker secreted by OBs, constitutes the main component of bone organic matrix and the primary extracellular matrix.[24–26] ALP is a recognized differentiation and histological marker for OBs; its activity reflects the degree of OB differentiation, with higher ALP activity indicating stronger osteogenic activity. OCN is a bone-specific noncollagenous protein synthesized by mature OBs that plays an important role in maintaining normal bone calcification. OCN promotes bone mineralization and is a specific marker of mature OBs.[27] Moreover, bFGF maintains the osteogenic properties of BMSCs, stimulates DNA synthesis, increases OCN levels in differentiated OBs, accelerates bone calcification, and promotes new bone formation. Additionally, bFGF induces chemotaxis of various cells in the vascular intima, promotes their migration and growth, and promotes neovascularization *in vivo* and *in vitro*. Therefore, bFGF is an important angiogenic factor.[28–30] Moreover, VEGF promotes neovascularization in the implant material and stimulates the migration and growth of vascular endothelial cells, thereby playing an important role in the regeneration and reconstruction of bone defects. Furthermore, VEGF promotes the migration of bone progenitor cells and stimulates the differentiation of primary OBs, which also play critical roles in the repair and reconstruction of bone defects.[31,33] Therefore, VEGF plays an important role in both neovascularization and bone regeneration. In this study, the expression levels of OGPs were detected using RT-PCR and western blotting. The relative expression levels of ALP, OCN, OPG, VEGF, bFGF, OPN, and type I collagen were markedly higher in group A than in group B. This suggests that osteogenic activity was greater in group A than in group B.

Although 3D printing technology has shown great potential in bone tissue engineering, there are still limitations in printing accuracy and in the complexity of structures that can be fabricated, and printing equipment and process parameters require further optimization. BMSCs often require additional surgical procedures for harvesting and are constrained by time, anatomical location, and tissue source. In contrast, induced pluripotent stem cells (iPSCs) possess pluripotent and multilineage differentiation capabilities similar to embryonic stem cells but without the ethical concerns or risk of immune rejection associated with these cells.[32] At present, iPSCs can be obtained through somatic reprogramming from autologous hosts, offering the possibility of obtaining mesenchymal stem cells via *in vitro* differentiation of iPSCs, thereby overcoming the limitations associated with traditional BMSCs.

5. Conclusion

In this study, a novel HA/ZrO_2 composite scaffold material was created using light-curing printing technology. The scaffold material exhibits nanoscale characteristics and an interconnected 3D structure, which are conducive to the growth of bone and blood vessels. Therefore, the material may effectively address the challenge of personalized bone defect repair. A key innovation of this study lies in the ability to customize the scaffold morphology to precisely match individual bone defects using 3D-printing technology. This approach enables the fabrication of highly biomimetic 3D porous structures with adjustable pore size, porosity, and connectivity, significantly enhancing OB adhesion, proliferation, and differentiation. Notably, BMP-2 is integrated into the composite scaffold material as an osteogenic inductive factor, which further enhances the osteogenic differentiation capacity of BMSCs. Overall, the composite scaffold material showed good cellular biocompatibility, excellent osteogenic efficacy, and satisfactory biomechanical strength, indicating its promising potential as a bone tissue repair material.

Acknowledgments

We thank the School of Materials Science and Engineering (Shanghai University) for preparing the novel porous gradient HA/ZrO2 scaffold material and providing information on its structure.

Funding

This work was supported by the Medical and Health Science and Technology Project in Zhejiang Province [2024KY261] and Zhejiang Natural Science Foundation Project (LQN25H270017).

Conflict of interest

The authors declare no conflict of interest.

Author contributions

Conceptualization: Tuo Wang and Huan-Huan Gao
Formal analysis: Can-Da Xu, Xiao-Long Huang
Investigation: Rui Qiu, Hua-Teng Zhou, Wei-Bin Du, Xi-Cheng Wei, Long-Bao Lv, Cai-Yin Xu
Methodology: Ren-Fu Quan, Rui Qiu
Supervision: Ren-Fu Quan, Rui Qiu
Writing–original draft: Rui Qiu
Writing–review & editing: Ren-Fu Quan, Jin-Fu Wang
All authors have read and approved the final manuscript.

Ethics approval and consent to participate

All animal procedures described were approved by the Committee of Kunming Institute of Zoology (KIZ) (production license number: SCXK-K2013-0005, research use license number: SYXK-K2013-0012). The animal experiment protocol was approved by the Institutional Animal Care and Use Committee of KIZ, Chinese Academy of Sciences, and was performed strictly following Chinese laws on animal experimentation. The feeding conformed to the standards of the animal feeding requirements set by KIZ.

Consent for publication

Not applicable.

Availability of data

The datasets generated during and/or analyzed during the current study are available from the corresponding author on reasonable request.

References

1. Dec P, Modrzejewski A, Pawlik A, Existing and novel biomaterials for bone tissue engineering. *Int J Mol Sci*. 2022:24:529. doi: 10.3390/ijms24010529
2. Jagadale S, Damle M, Joshi MG. Bone tissue engineering: from biomaterials to clinical trials. *Adv Exp Med Biol*. 2025;1479:73-115. doi: 10.1007/5584_2024_841
3. Brachet A, Bełżek A, Furtak D. *et al*. Application of 3D printing in bone grafts. *Cells*. 2023;12:859. doi: 10.3390/cells12060859
4. Maresca JA, DeMel DC, Wagner GA, *et al*. Three-dimensional bioprinting applications for bone tissue engineering. *Cells*. 2023;12:1230.
5. Chatzipetros E, Damaskos S, Tosios KI, *et al*. The effect of nano-hydroxyapatite/chitosan scaffolds on rat calvarial defects for bone regeneration. *Int J Implant Dent*. 2021;7:40. doi: 10.1186/s40729-021-00327-w
6. Quan RF, Tang YH, Huang ZM, *et al*. Difference of adherence, proliferation and osteogenesis of mesenchymal stem cells cultured on different HA/ZrO2 composites. *Chin J Traumatol*. 2012;15:131-139.
7. Ingwersen LC, Frank M, Naujokat H, *et al*. BMP-2 long-term stimulation of human pre-osteoblasts induces osteogenic differentiation and promotes transdifferentiation and bone remodeling processes. *Int J Mol Sci*. 2022;23:3077. doi: 10.3390/ijms23063077
8. Grosso A, Lunger A, Burger MG, *et al*. VEGF dose controls the coupling of angiogenesis and osteogenesis in engineered bone. *NPJ Regen Med*. 2023;8:15. doi: 10.1038/s41536-023-00288-1
9. Gorskaya YF, Danilova TA, Karyagina AS, *et al*. Effects of combined treatment with complex S. typhimurium antigens and factors stimulating osteogenesis (curettage, BMP-2) on multipotent bone marrow stromal cells and serum concentration of cytokines in CBA mice. *Bull Exp Biol Med*. 2015;158:465-470. doi: 10.1007/s10517-015-2786-z
10. Kong D, Shi Y, Gao Y, *et al*. Preparation of BMP-2 loaded MPEG-PCL microspheres and evaluation of their bone repair properties. *Biomed Pharmacother.* 2020;130: 110516. doi: 10.1016/j.biopha.2020.110516
11. Arthur A, Gronthos S. Clinical application of bone marrow mesenchymal stem/stromal cells to repair skeletal tissue. *Int J Mol Sci*. 2020;21:9759. doi: 10.3390/ijms21249759
12. Gholami Farashah MS, Javadi M, Mohammadi A, *et al*. Bone marrow mesenchymal stem cell's exosomes as key nanoparticles in osteogenesis and bone regeneration: specific capacity based on cell type. *Mol Biol Rep*. 2022;49:12203-12218. doi: 10.1007/s11033-022-07807-1
13. Yazdanpanah Z, Sharma NK, Raquin A, *et al*. Printing tissue-engineered scaffolds made of polycaprolactone and nano-hydroxyapatite with mechanical properties appropriate for trabecular bone substitutes. *Biomed Eng Online*. 2023; 22:73. doi: 10.1186/s12938-023-01135-6
14. Rajabi M, Cabral JD, Saunderson S, *et al*. Development and optimisation of hydroxyapatite-polyethylene glycol diacrylate hydrogel inks for 3D printing of bone tissue engineered scaffolds. *Biomed Mater*. 2023;18(6). doi: 10.1088/1748-605X/acf90a
15. Bahraminasab M, Talebi A, Doostmohammadi N, *et al*. The healing of bone defects by cell-free and stem cell-seeded 3D-printed PLA tissue-engineered scaffolds. *J Orthop Surg Res*. 2022;17:320. doi: 10.1186/s13018-022-03213-2
16. Zalewska J, Przekora A, Pałka K, *et al*. Gypsum-related compensation of ions uptake by highly porous hydroxyapatite ceramics: – consequences for osteoblasts growth and proliferation. *Biomater Adv.* 2022;133:112665. doi: 10.1016/j.msec.2022.112665
17. Ostrowska B, Di Luca A, Szlazak K, *et al*. Influence of internal pore architecture on biological and mechanical properties of three-dimensional fiber deposited scaffolds for bone regeneration. *J Biomed Mater Res A*. 2016;104:991-1001. doi: 10.1002/jbm.a.35637

18. Shao RX, Quan RF, Huang XL, *et al*. Evaluation of porous gradient hydroxyapatite/zirconia composites for repair of lumbar vertebra defect in dogs. *J Biomater Appl*. 2016;30:1312-1321.
doi: 10.1177/0885328215627616

19. Julien A, Perrin S, Martínez-Sarrà E, *et al*. Skeletal stem/progenitor cells in periosteum and skeletal muscle share a common molecular response to bone injury. *J Bone Miner Res*. 2022;37:1545-1561.
doi: 10.1002/jbmr.4616

20. Salamanca E, Wu YF, Aung LM, *et al*. Allylamine coating on zirconia dental implant surface promotes osteogenic differentiation *in vitro* and accelerates osseointegration *in vivo*. *Clin Oral Implants Res*. 2024;35:1101-1113.
doi: 10.1111/clr.14300

21. Kim J, Kang IG, Cheon KH, *et al*. Stable sol-gel hydroxyapatite coating on zirconia dental implant for improved osseointegration. *J Mater Sci Mater Med*. 2021;32:81.
doi: 10.1007/s10856-021-06550-6

22. Kusuyama J, Amir MS, Albertson BG, *et al*. JNK inactivation suppresses osteogenic differentiation, but robustly induces osteopontin expression in osteoblasts through the induction of inhibitor of DNA binding 4 (Id4). *FASEB J*. 2019;33:7331-7347.
doi: 10.1096/fj.201802465R

23. Mardiyantoro F, Chiba N, Seong CH, *et al*. Two-sided function of osteopontin during osteoblast differentiation. *J Biochem*. 2025;177:121-131.
doi: 10.1093/jb/mvae080

24. Selvaraj V, Sekaran S, Dhanasekaran A, *et al*. Type 1 collagen: synthesis, structure and key functions in bone mineralization. *Differentiation*. 2024;136:100757.
doi: 10.1016/j.diff.2024.100757

25. Asakura T, Diep TTT, Ueda Y, *et al*. Analysis of the effect of human type I collagen-derived peptide on bone regenerative capacity and comparison with various collagen materials *in vivo*. *Medicina (Kaunas)*. 2025;61:57.
doi: 10.3390/medicina61010057

26. Tateno A, Asano M, Akita D, *et al*. Transplantation of dedifferentiated fat cells combined with a biodegradable type I collagen-recombinant peptide scaffold for critical-size bone defects in rats. *J Oral Sci*. 2019;61:534-538.
doi: 10.2334/josnusd.18-0458

27. Vimalraj S. Alkaline phosphatase: structure, expression and its function in bone mineralization. *Gene*. 2020;754:144855.

28. Wu H, Yin G, Pu X, *et al*. Inhibitory effects of combined bone morphogenetic protein 2, vascular endothelial growth factor, and basic fibroblast growth factor on osteoclast differentiation and activity. *Tissue Eng Part A*. 2021;27:1387-1398.
doi: 10.1089/ten.TEA.2020.0325

29. Nakamichi M, Akishima-Fukasawa Y, Fujisawa C, *et al*. Basic fibroblast growth factor induces angiogenic properties of fibrocytes to stimulate vascular formation during wound healing. *Am J Pathol*. 2016;186:3203-3216.
doi: 10.1016/j.ajpath.2016.08.015

30. Pasanen S, Mootha A, Hirata I, *et al*. Enhanced growth of bone marrow-derived mesenchymal stem cells on the microcarriers tethered with engineered basic fibroblast growth factor. *Biotechnol J*. 2025;20:e70057.
doi: 10.1002/biot.70057

31. Hu K, Olsen BR. Osteoblast-derived VEGF regulates osteoblast differentiation and bone formation during bone repair. *J Clin Invest*. 2016;126:509-526.
doi: 10.1172/JCI82585

32. Veraitch O, Mabuchi Y, Matsuzaki Y, *et al*. Induction of hair follicle dermal papilla cell properties in human induced pluripotent stem cell-derived multipotent LNGFR(+)THY-1(+) mesenchymal cells. *Sci Rep*. 2017;7:42777.
doi: 10.1038/srep42777